Silicene, Siloxene, or Silicane? Revealing the Structure and Optical Properties of Silicon Nanosheets Derived from Calcium Disilicide

Bradley J. Ryan,[†] Michael P. Hanrahan,[‡,§] Yujie Wang,[†,⊥] Utkarsh Ramesh,[†,⊥] Charles K. A. Nyamekye,[‡,§] Rainie D. Nelson,[†] Zhaoyu Liu,[§,∥] Chuankun Huang,[§,∥] Bevan Whitehead,[§] Jigang Wang,[§,∥] Luke T. Roling,[†] Emily A. Smith,[‡,§] Aaron J. Rossini,[‡,§] and Matthew G. Panthani*,[†]

[†]Department of Chemical and Biological Engineering, Iowa State University, Ames, Iowa 50011, United States
[‡]Department of Chemistry, Iowa State University, Ames, Iowa 50011, United States
[§]U.S. Department of Energy, Ames Laboratory, Ames, Iowa 50011, United States
[∥]Department of Physics and Astronomy, Iowa State University, Ames, Iowa 50011, United States

S *Supporting Information*

ABSTRACT: Si-nanosheets (Si-NSs) have recently attracted considerable attention due to their potential as next-generation materials for electronic, optoelectronic, spintronic, and catalytic applications. Even though monolayer Si-NSs were first synthesized over 150 years ago via topotactic deintercalation of CaSi$_2$, there is a lack of consensus within the literature regarding the structure and optical properties of this material. Herein, we provide conclusive evidence of the structural and chemical properties of Si-NSs produced by the deintercalation of CaSi$_2$ with cold (~−30 °C) aqueous HCl and characterize their optical properties. We use a wide range of techniques, including XRD, FTIR, Raman, solid-state NMR, SEM, TEM, EDS, XPS, diffuse reflectance absorbance, steady-state photoluminescence, time-resolved photoluminescence, and thermal decomposition; when they are combined together, these techniques enable unique insight into the structural and optical properties of the Si-NSs. Additionally, we support the experimental findings with density functional theory (DFT) calculations to simulate FTIR, Raman, solid-state NMR, interband electronic transitions, and band structures. We determined that the Si-NSs consist of buckled Si monolayers that are primarily monohydride terminated. We characterize the nanosheet optical properties, finding they have a band gap of ~2.5 eV with direct-like behavior and an estimated quantum yield of ~9%. Given the technological importance of Si, these results are encouraging for a variety of optoelectronic technologies, such as phosphors, light-emitting diodes, and CMOS-compatible photonics. Our results provide critical structural and optical properties to help guide the research community in integrating Si-NSs into optoelectronic and quantum devices.
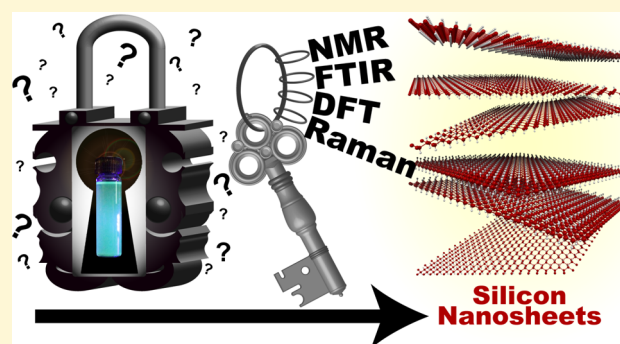
INTRODUCTION

Recent progress in the area of two-dimensional (2D) materials such as graphene[1] and MoS$_2$[2] has sparked interest within the research community due to extraordinary properties that have potential for transformative technologies. 2D materials offer properties superior to those of their bulk counterparts, with higher photosensitivity,[3] tunable band structures and band gaps,[4,5] and increased exciton annihilation efficiency.[6−8] 2D semiconductors have immense potential to satisfy the need to decrease the size of microelectronic components; however, there are limitations on material composition due to desires to integrate materials which are currently established in our electronics infrastructure. 2D Si-nanosheets (Si-NSs) have properties that may add new optical and electronic functionality to semiconductors while being comprised of

elements that allow for preserving the existing infrastructure on which our microelectronics technology resides.

Prior studies have reported the synthesis of monolayer Si-NSs and investigated their optical properties. These reports include structures such as silicane (Si$_6$H$_6$ or layered polysilane)[9] and siloxene[10−13] (Si$_6$H$_3$(OH)$_3$), both synthesized via topotactic deintercalation of Ca from CaSi$_2$ using aqueous HCl. In the silicane structure, intercalated Ca atoms are removed, leaving a buckled Si backbone with each Si atom terminated with H.[12] There are various reported structures of siloxene: Wöhler siloxene (i.e., *cis*-hydroxysilicane) is terminated with OH on one side and H on the other,[14] while

Kautsky siloxene consists of Si_6H_6 rings connected by SiOSi bridges or as 1D Si—Si chains connected by SiOSi bridges.[15,16] However, the literature lacks conclusive evidence to sufficiently describe the structure and coordination chemistry of these Si-NSs.

There have been several reports on the synthesis of Si-NSs obtained from the deintercalation of $CaSi_2$ with aqueous HCl;[13,17−41] however, the reported structures have been inconsistent. For example, recent reports have indicated that deintercalation of $CaSi_2$ leads to a Si-NS structure that can be described by a Si backbone that is terminated with H, O, OH, and alkyl groups; conversely, other reports have concluded that deintercalation leads to Kautsky-type siloxene or even 2D sheets consisting of a silicon oxide framework that is terminated with OH groups. Other reports claim that the product is hydrogen-terminated Si-NSs. These discrepancies motivated our work to explore the structural properties of the Si-NSs obtained from deintercalating $CaSi_2$ with aqueous HCl.

In this work, we characterize the structural and optical properties of Si-NSs using a variety of diffraction, spectroscopic, thermal, and microscopy techniques to elucidate the structure, composition, and optical properties of the Si-NSs. We use density functional theory (DFT)[42−45] calculations of FTIR, Raman, solid-state NMR, interband electronic transitions, and band structures to support our experimental conclusions. The results of this study suggest that the Si-NSs consist of a buckled Si monolayer that is mostly monohydride terminated, resembling silicane, with a relatively small quantity of chloride and hydroxide termination.

■ RESULTS AND DISCUSSION

The Si-NSs were synthesized by deintercalating $CaSi_2$ in aqueous HCl at ~−30 °C. Scanning electron microscopy (SEM) images of the Si-NSs (Figure 1c,d) reveal a morphology that resembles loosely stacked sheets that are not atomically registered with each other, consistent with deintercalation of Ca^{2+}. This lack of registry prevents isolation of extended crystals of stacked Si-NSs, and is corroborated by the photograph in Figure 1a, which shows a large volume expansion accompanying deintercalation, indicating an increase in Si-NS interlayer separation. Transmission electron microscopy (TEM) images show the presence of stacks and few-layer wrinkled sheets (Figure 1e and Figure S1). The decrease in particle size after deintercalation likely arises from agitation provided by stirring during the deintercalation step (Figure 1b,c).

Powder X-ray diffraction (XRD) indicates that impurities of bulk-Si and α-FeSi$_2$ exist within the commercially sourced $CaSi_2$ (Figure S2). The presence of Fe is confirmed with energy-dispersive X-ray spectroscopy (EDS) (Figures S3−S10). No XRD reflections exist other than those corresponding to the impurities, suggesting that the Si-NSs do not exhibit commensurate registry, unlike the germanium analogue;[46] this demonstrates the difficulties in isolating single crystals of stacks of the Si-NSs. Large (ca. 1−100 μm) chunks of bulk-Si are observed in the deintercalated product in both SEM (Figure S8) and bright−bright field optical images (Figure S17a,b). $CaCl_2$ is not observed with XRD.

We used Raman spectroscopy to characterize the Si-NSs (Figure 2a and Figures S14 and S15) and $CaSi_2$ (Figure S17). Peak assignments were based upon the literature and validated with DFT. Si-NSs exhibit Raman modes at 375 (2D-Si planes),[35,47,48] 489 (2D-Si$_6$ rings),[35,47] 632 (SiH$_n$),[47,49] 726
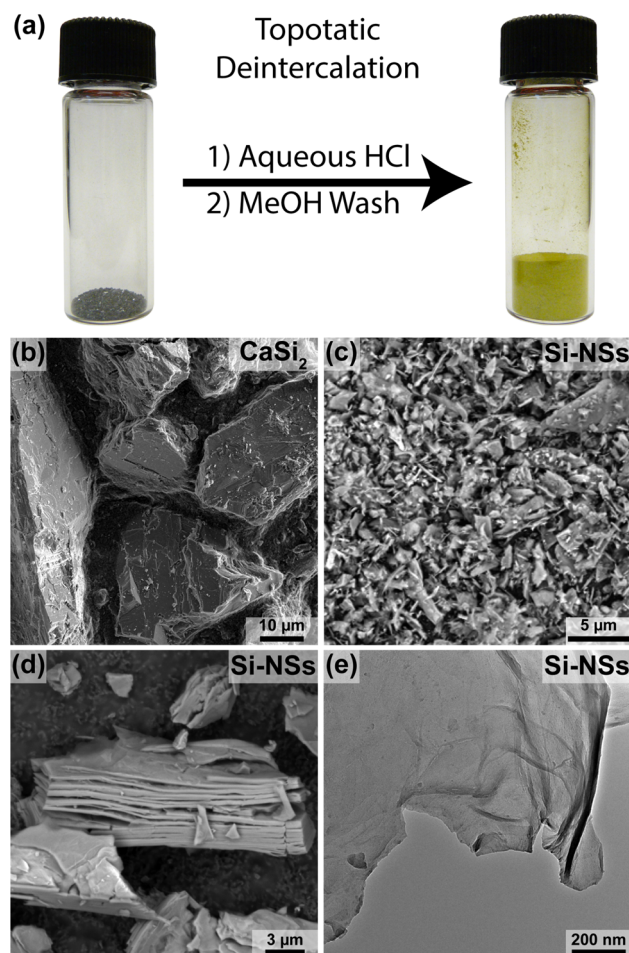

Figure 1. (a) Reaction schematic with images before and after deintercalation. The volume of powders is representative of the reaction. SEM images of (b) $CaSi_2$, (c) representative area of the Si-NSs, and (d) selected area of large Si-NSs. (e) TEM image of a few-layer-thick stack of Si-NSs.

(SiH),[50] ~900 (SiH$_2$ and/or SiOH), 2126 (SiH$_n$),[49−51] and 2248 cm^{-1} (OSiH$_n$).[52] The peak at 375 cm^{-1} is likely Si—Si vibrations, which also exist in $CaSi_2$ at 387 cm^{-1};[35,47,48] this is confirmed by DFT (see GIF files in the Supporting Information for visualization of the vibrational modes). The peaks at 375 and 489 cm^{-1} are red-shifted in comparison to $CaSi_2$, which is characteristic of phonon confinement effects that are expected to result from increased inter-sheet separation. The peak at 489 cm^{-1} agrees well with previous theoretical results of monolayer Si.[53] The peaks at 511 and ~945 cm^{-1} are attributed to bulk-Si impurities.[54−57] Weak SiOH features are observed between ~3300 and 3800 cm^{-1} (Figure S14b),[58,59] which likely arise from the Si-NSs and the Si-containing impurities.

FTIR spectra are shown in Figure 2b. Experimental (DFT) silicon-hydride modes occur at 2108 (2136),[40,47] 897 (897/903),[60] 877,[47,61] 742,[47] 635 (601),[40,60,61] and 512 (511) cm^{-1};[62] the peaks at 897 and 877 cm^{-1} correspond to SiH$_2$ modes.[47,60,61] Many previous reports attributed the peak at ~512 cm^{-1} to Si—Si, contrary to our work and a prior isotope vibrational study;[62] DFT demonstrates this peak as a wag of SiH (see GIF files in the Supporting Information for visualization of the vibrational modes). Oxygen-containing FTIR modes occur at 797 (SiO),[62] 1027 (SiOSi),[40,47] 2250

(O_3SiH),[40,47] and 3595 cm^{-1} (SiOH).[63-66] Features at 3362 and 1631 cm^{-1} are attributed to intercalated and/or adsorbed H_2O; Raman spectra exhibit no such features, as Raman scattering of H_2O is weak.[67] Thermal decomposition also suggests the presence of H_2O (Figures S21 and S22). DFT predicts SiOH and SiO modes at 3740 and 774 cm^{-1}, agreeing with the literature.[65,68] The only common SiO feature in Raman and FTIR is the feature at ~900 cm^{-1}, which might also arise from SiH_2 modes, as suggested by DFT. The CH_x features observed at ca. 1360-1460 and 2850-3000 cm^{-1} do not arise from $SiOCH_3$, as the spectrum lacks the strong CO stretch at ~1182 cm^{-1}.[69]

We used DFT to simulate the vibrational modes of the Si-NSs. Several structures were geometrically relaxed into their
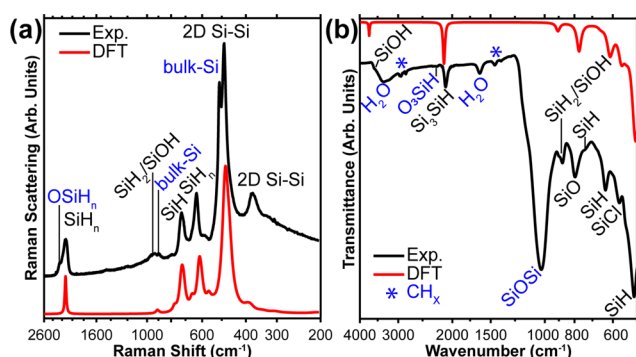
Figure 2. (a) Raman and (b) FTIR spectra of the Si-NSs. See Table S2 (Table S3) for complete Raman (FTIR) peak assignments. Peaks labeled in blue were intentionally not modeled with DFT. Note that the x axes are plotted on a log scale, increasing the apparent width of all peaks at low wavenumber while compressing the width of all peaks at high wavenumber. Black and red curves are experimental data and DFT simulations, respectively.

most thermodynamically stable configuration. We hypothesized that SiH (middle of a sheet), SiH_2 (edge of a sheet), SiH_3 (corner of a sheet), SiOH, and SiCl functional groups could be attached to the Si-NSs; this hypothesis was based on our NMR data (vide infra) and knowledge of finite sheets (edges and corners). These structures consisted of monolayer Si-NSs containing $Si_{4-n}SiH_n$ ($1 \leq n \leq 3$), $Si_{3-n}SiH_nCl$ ($0 \leq n \leq 2$), and/or SiOH groups (Figure S24). For each structure, the spatial location of each ion was allowed to relax, minimizing the forces on each atom and the overall energy of the system as defined by the Kohn–Sham[42] equations. The DFT-simulated Raman and FTIR spectra (Figure 2) show a linear combination of nanosheets containing SiH, SiH_2, SiCl, and SiOH groups (also see Figure S25). Note that the same linear combination of structures was used for Raman and FTIR spectra.

A comparison of experimental and DFT data suggests that there are few SiH_2 and SiH_3 groups relative to SiH. DFT suggests the FTIR feature at 572 cm^{-1} corresponds to SiCl, agreeing well with prior nanocrystal work.[70] The presence of Cl is confirmed with EDS, X-ray photoelectron spectroscopy (XPS), and FTIR analysis of gaseous thermal decomposition byproducts (Figures S5-S10, S20, and S21 and S22, respectively). Thermal decomposition shows an evolution of HCl(g) at ~350 °C. We roughly estimate the ratio of Si:Cl to be 6.7:1, agreeing well with a prior report;[40] however, it is unclear if the presence of Cl solely arises from SiCl or if intercalated HCl also contributes to the Cl signal. The

presence of residual HCl or $CaCl_2 \cdot xH_2O$ is not observed in Raman[71] or FTIR (Figure S18).

While the FTIR data exhibit an intense SiOSi feature, it is important to note that the relative intensity of an FTIR feature does not correlate to the relative concentration of the bonds participating in that particular mode. The intensity is, however, directly proportional to the square of the change in dipole moment (induced by the IR-excited phonon) with respect to the normal-mode coordinate.[72] For a given vibrational mode, i, the intensity of an FTIR feature, I_i^{FTIR}, can be calculated by squaring the sum over all atoms, the product of the Born effective charge tensor,[73] $Z_{\alpha,\beta}^*$, and the atomic-displacement vibrational eigenvector, $\mathbf{e}_\beta$, as shown in eq 1.

$$I_i^{FTIR} = \sum_{\alpha=1}^{3} \left[\sum_{s=1}^{m} \sum_{\beta=1}^{3} Z_{\alpha,\beta}^*(s)\mathbf{e}_\beta(s) \right]^2 \tag{1}$$

In eq 1, $Z_{\alpha,\beta}^*$ is the proportionality constant relating the polarization in the α direction induced by the displacement of atoms in the β direction, $\mathbf{e}_\beta$ is the spatial displacement of atoms along the vibrational coordinate, and s is an index running over all atoms belonging to the ith vibrational mode. Thus, the FTIR intensity is a function of the number of atoms involved in a vibrational mode, the magnitude of the distance each atom moves within a vibration, and the magnitude of the elements of the Born effective charge tensor. In Table S5, the Born effective charge tensors for each atom for characteristic vibrations are shown for α-quartz, silane, and cis-hydroxysilicane.

For SiO bonds, the relatively large magnitude of the diagonal components of $Z_{\alpha,\beta}^*(Si)$ and $Z_{\alpha,\beta}^*(O)$ gives rise to intense FTIR features. We calculate that, on a unit cell basis, the intensities of the vibrational modes of SiO and SiOH in cis-hydroxysilicane at 773 and 3741 cm^{-1} are ca. 5 and 2 times greater than those of its SiH mode at 2118 cm^{-1}, respectively. To this end, we compared the DFT predictions of FTIR intensities of the SiO features in α-quartz to the characteristic modes in silane and cis-hydroxysilicane. These results demonstrate that, on a unit cell basis, the FTIR-active SiO modes in α-quartz are ca. 9 and 29 times greater than the SiH features in silane at 511 and 2136 cm^{-1}, respectively. Similarly, the predicted SiO intensities of α-quartz are ca. 14, 70, and 29 times greater than the SiO, SiH, and SiOH features in cis-hydroxysilicane at 773, 2118, 3741 cm^{-1}, respectively. Thus, we conclude that the intense SiOSi feature arises from the relatively large induced dipole moment of SiO bonds in this material—not from a high concentration of SiO bonds. The SiOSi bonds likely originate from oxidation during deintercalation and washing steps.

High-resolution magic angle spinning (MAS) ^1H and ^{29}Si solid-state NMR spectroscopy were used to investigate the structure of the Si-NSs. The ^1H NMR signals at 3.9 and 6.0 ppm are assigned to Si_3SiH,[74-76] while the signal at 1.3 ppm is likely Si_3SiOH (Figure 3a). A $^1H-^1H$ dipolar double quantum single quantum homonuclear correlation (DQ-SQ) spectrum[77] demonstrates SiH_x species correlate to themselves and all other ^1H signals, indicating that all of these hydrogen sites are proximate within a Si-NS (Figure S26), consistent with the 2D ^{29}Si scalar DQ-SQ spectrum (vide infra).

We justify the Si_3SiOH assignment in the following. The assignment at 1.3 ppm is in good agreement with isolated silanol groups on the surface of silica, which resonate near 1.8
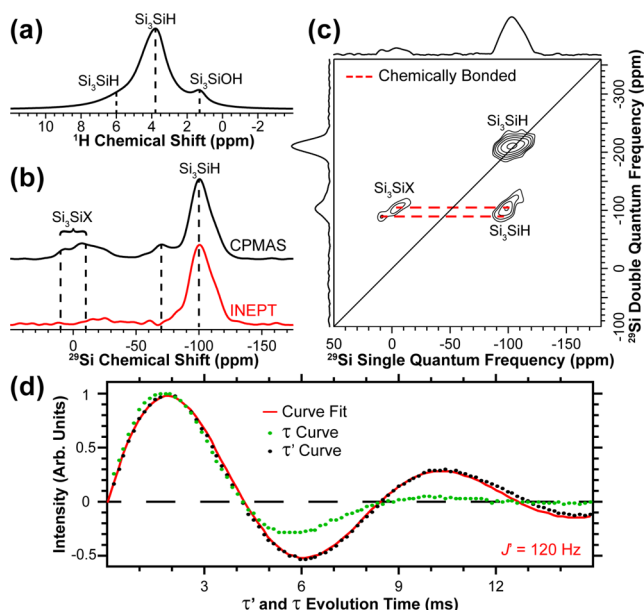
Figure 3. (a) MAS ^{1}H solid-state NMR spectrum (ν_{rot} = 25 kHz). (b) Comparison of CPMAS (CP contact time of 6 ms) and ^{1}H–^{29}Si refocused INEPT (τ' and τ mixing times of 1.44 ms). Dashed lines are shown to guide the eye. (c) Natural-abundance ^{29}Si–^{29}Si scalar DQ-SQ spectrum acquired with $\tau_{1/4J}$ (MAS frequency) of 6 ms (10 kHz). Dashed red lines indicate chemically bonded ^{29}Si spins. (d) INEPT τ and τ' J-evolution curves with a fit of the τ' curve to determine $^1J_{SiH}$.[74]

ppm. Further, the 1.3 ppm ^{1}H signal is absent from the ^{1}H–^{29}Si INEPT HETCOR spectra (which uses a single-bond ^{1}H–^{29}Si J coupling for the coherence transfer), and the signal is weakly visible in the ^{1}H–^{29}Si CP-HETCOR spectrum recorded with a long contact time of 6 ms; both of these observations confirm that this ^{1}H signal does not arise from a hydrogen directly bonded to silicon. Finally, this assignment is supported by DFT calculations (see the Supporting Information for details). We find that a Si-NS containing SiH and SiOH groups (Figure S30c) have predicted chemical shifts of 2.5–3.9 and 0.13 ppm, respectively, while the experimental values correspond to 3.9 and 6.0 and 1.3 ppm, respectively. Importantly, we point out the similar offset in the experimental and DFT-calculated chemical shifts for the SiH and SiOH groups.

1D and 2D ^{29}Si NMR spectra were obtained with ^{1}H–^{29}Si cross-polarization (CP) or ^{1}H–^{29}Si insensitive nuclei enhanced by polarization transfer (INEPT)[78] (Figure 3b and Figures S27 and S28). The 1D ^{1}H–^{29}Si CPMAS spectrum exhibits broad, low-intensity ^{29}Si NMR signals centered at isotropic chemical shifts of ca. ±10, −70, and a broad intense signal at −100 ppm (Figure 3c). These signals were assigned with various 1D and 2D NMR experiments. The 1D INEPT spectrum and 2D ^{1}H–^{29}Si INEPT-HETCOR spectrum (Figure S28) shows correlations between ^{1}H (^{29}Si) signals at 3.9 ppm (−100 ppm), suggesting that the most intense ^{1}H and ^{29}Si NMR signals arise from silicon hydrides. One-bond ^{1}H–^{29}Si J couplings ($^1J_{SiH}$) and the multiplicity of the hydride groups were determined by varying the INEPT J-coupling evolution times (τ' and τ) and monitoring the oscillation of the INEPT NMR signal (Figure 3d).[74] The similarity of the τ' and τ curves directly confirms that the NSs primarily consist of monohydrides. A fit of the τ' curve yields a scaled ^{1}H–^{29}Si J coupling of 120 Hz, which corresponds to $^1J_{SiH} \approx$ 198 Hz after correcting for the ^{1}H

homonuclear decoupling scaling factor. A $^1J_{SiH}$ coupling of 198 Hz is consistent with the $^1J_{SiH}$ value previously measured for surface hydride groups on Si-NCs[74] and small-molecule silanes.[79]

A direct excitation (DE) ^{29}Si NMR spectrum obtained with a 30 min recycle delay showed signals similar to those in the CPMAS and INEPT spectra and a new intense ^{29}Si signal at −80 ppm attributed to bulk-Si impurities (Figure S29 and Table S7).[80] Integration of the DE NMR spectrum suggests that ∼30% of the NMR signal is from bulk-Si impurities; however, we note that this spectrum is not absolutely quantitative because ^{29}Si can have spin−lattice relaxation times (T_1) between minutes and days.

A 2D ^{29}Si–^{29}Si scalar DQ-SQ spectrum was obtained with the refocused INADEQUATE pulse sequence[81] to determine whether the ^{29}Si signals at ±10 and −70 ppm arise from Si atoms within the NSs (Figure 3c). The DQ-SQ spectrum shows intense autocorrelation at −200 (−100) ppm in the DQ (SQ) dimensions, confirming Si−Si bonds between SiH groups within the sheets. The INADEQUATE spectrum also shows that signals at ±10 ppm arise from Si atoms that are directly bonded to SiH groups. The ^{29}Si signals at ±10 ppm are absent from 1D and 2D ^{1}H–^{29}Si INEPT spectra, suggesting that they lack SiH bonds. Thus, we conclude that the ^{29}Si signals at ±10 ppm likely correspond to Si$_3$SiX groups (where X ≠ H). These signals could arise from Si$_3$SiCl or Si$_3$SiOH; however, no autocorrelations are observed for the Si$_3$SiX signals, suggesting that any SiX groups are isolated within the sheets and there are few XSi−SiX bonds. Chemical shifts were predicted with DFT on structural models similar to those used for the predictions of FTIR and Raman spectra. The calculated and experimental chemical shifts are in good agreement, confirming the NMR assignments (see Figures S30−S32 and Tables S8 and S9).

To probe the interactions of electromagnetic radiation with silicane, we compared experimental absorbance data with DFT predictions of the extinction coefficient, ε, which is derived from the dielectric function, $\varepsilon_{\alpha\beta}$. The dielectric function is a complex-valued 3 × 3 tensor with real and imaginary parts, $\varepsilon_{\alpha\beta}^{(1)}$ and $\varepsilon_{\alpha\beta}^{(2)}$, respectively, such that $\varepsilon_{\alpha\beta}(E) = \varepsilon_{\alpha\beta}^{(1)}(E) + i\varepsilon_{\alpha\beta}^{(2)}(E)$. Here, α is the direction of the dielectric response due to an electric field applied in the β direction. The imaginary portion of $\varepsilon_{\alpha\beta}$ is calculated by eq 2 and depends on the energy of the electromagnetic radiation, E.

$$\varepsilon_{\alpha\beta}^{(2)}(E) = \frac{4\pi^2 e^2}{V} \lim_{q \to 0} \frac{1}{q^2} \sum_{c,v,\mathbf{k}} [2\omega_{\mathbf{k}}\delta(E_{c\mathbf{k}} - E_{v\mathbf{k}} - E)$$

$$\times \langle u_{c\mathbf{k}+\mathbf{qe}_\alpha}|u_{v\mathbf{k}}\rangle\langle u_{v\mathbf{k}}|u_{c\mathbf{k}+\mathbf{qe}_\beta}\rangle] \quad (2)$$

The summation runs over all conduction and valence bands for all wave vectors within the first Brillouin zone (c, v, and $\mathbf{k}$, respectively). $\mathbf{q}$ is the Bloch wave vector of the incident wave, V is the volume of the unit cell, $\omega_{\mathbf{k}}$ is the wavelength of the incident wave, and δ is the Dirac delta function. The product of the bra-ket terms can intuitively be thought of as the probability of an electron being excited from a conduction to a valence band at a wave vector, $\mathbf{k}$. The periodic coefficients of the Bloch waves are represented by $u_{c\mathbf{k}}$ and $u_{v\mathbf{k}}$. The unit vectors along the three principal directions are represented by $\mathbf{e}_\alpha$ and $\mathbf{e}_\beta$.

Qualitatively, eq 2 sums over all bands in the first Brillouin zone, all transitions from a conduction to a valence band with

an energy equal to that of the incident electromagnetic radiation, weighted by the probability of the transition occurring. With $\varepsilon_{\alpha\beta}^{(2)}$, the real portion of the dielectric function, $\varepsilon_{\alpha\beta}^{(1)}$, can be calculated with the Kramers–Kronig transformation. The extinction coefficient (Figure 4a) is calculated
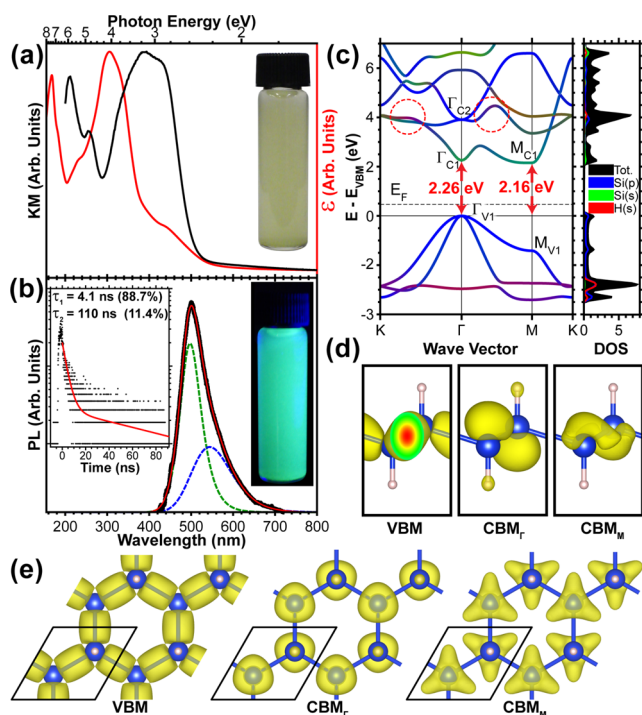
Figure 4. (a) KM (black) and simulated extinction coefficient (red). The photo inset is of the sample dispersed in methanol under ambient lighting. (b) Photoluminescence and its deconvolution. The excitation wavelength is 375 nm, the photo inset is of the dispersed sample under UV illumination, and the graph inset is TRPL. Green and blue dashed lines are the peak deconvolution, and the solid red line is the sum of the peak fits. (c) Band structure and projected density of states (pDOS). The colors of each band at a given wave vector quantitatively depict the deconvolution of the pDOS into the hybridization of each band; Si(p), Si(s), and H(s) are shown in blue, green, and red, respectively. The Fermi energy (E_F) is shown with a black dashed line. Energies are relative to the VBM. Select transitions corresponding to the text are labeled. The real-space orbitals at the valence band maximum (VBM) and conduction band minimum at Γ and M (CBM$_\Gamma$, CBM$_M$, respectively) viewed down the a and c axes are shown in (d) and (e), respectively. The unit cell is shown in black, and electron density isosurfaces are plotted at 0.0844 Å^{-3}. The red circles in (c) indicate the contribution of hydrogen, which is hypothesized to decrease the energy of the CBM$_\Gamma$.

with eq 3. Here, we assumed that the experimental sample is comparable to a uniformly dispersed sample without any preferential direction, and as such, we calculated the direction-averaged extinction coefficient by using the trace of $\varepsilon_{\alpha\beta}^{(1)}$ and $\varepsilon_{\alpha\beta}^{(2)}$.

$$\varepsilon = \sqrt{0.5\left(-\mathrm{Tr}(\varepsilon_{\alpha\beta}^{(1)}) + \sqrt{(\mathrm{Tr}(\varepsilon_{\alpha\beta}^{(1)}))^2 + (\mathrm{Tr}(\varepsilon_{\alpha\beta}^{(2)}))^2}\right)}$$

$$(3)$$

A Kubelka–Munk (KM) transformation of diffuse reflectance demonstrates that the Si-NSs have optical features similar to those of previous reports (Figure 4a).[11,19,82] Tauc analysis of the KM data (Figure S33) indicates a direct band gap of 2.53 eV; DFT predicts an indirect band gap of 2.16 eV

that is energetically close to a direct transition at 2.26 eV. DFT predictions of the extinction coefficient (Figure 4a) demonstrate a shoulder between ~2.3 and 3 eV—a feature not present in the experimental KM data—which is attributed to the conduction band with energies below ~3 eV (Figure 4c). The onset of ε is attributed to the direct transition $\Gamma_{V1} \rightarrow \Gamma_{C1}$. The sharp increase of ε at ~3.2 eV correlates to the increased density of states (DOS) at ~3.2−4.1 eV and the optically allowed transition $M_{V1} \rightarrow M_{C1}$ (transition of 3.6 eV). We therefore conclude that the experimental Si-NSs have a larger DOS at the absorption onset in comparison to the simulated models; we speculate that this increased DOS arises from defects. It has been reported that hydroxyl groups[13,28,32,83−85] and chlorination[86,87] can induce a direct transition within Si-NSs (also see Figure S34c). We ascribe the KM peak at 3.2 eV to the electronic transition associated with the Si$_6$ framework,[82] corresponding to the ε peak at ~4 eV, arising from the direct transition near M and the Si(p) → Si(p) transition from $\Gamma_{V1} \rightarrow \Gamma_{C2}$ (transition of 3.91 eV).

Photoluminescence (PL) spectra were collected from a dispersion of Si-NSs in methanol (Figure 4b). The PL maximum occurs near the absorption onset, which is characteristic of direct band gap behavior. The peak is centered at 500 nm (2.48 eV), closely matching the band gap estimated using Tauc analysis, assuming a direct band gap (Figure S33). The PL spectrum is asymmetric and has a full width at half-maximum (fwhm) of ~0.37 eV. By fitting the PL to two Gaussian−Lorentz product distributions, we deconvoluted the spectrum into two distributions: a higher energy peak centered at 498 nm with a fwhm of 0.31 eV, comprising 64% of the total curve, and a lower energy peak centered at 543.9 nm with a fwhm of 0.48 eV, comprising 36% of the total curve; see Table S10 for peak fitting parameters. Time-resolved PL (TRPL) suggests a biexponential decay, with a shorter lifetime of ~4.1 ns and a longer lifetime of 110 ns (Figure 4b, inset); such short lifetimes provide additional evidence of direct band gap emission.[88]

We estimate the PL quantum yield (PLQY) of a dispersion of the Si-NSs in methanol to be ~9%; however, the preparation of nonscattering dispersions limits our ability to accurately determine this value. This agrees well with a previous study that also determined a PLQY of 9%.[17] Further experimental investigations on the influence of terminal SiOH and SiCl groups are needed to gain a better understanding of the origin of emission.

Figure 4c shows the band structure and projected density of states (pDOS) of silicane. The color of each band enables visualization of the hybridization of each band at a given wave vector. The Si(p) orbitals (blue line in the pDOS) contain the p_x, p_y, and p_z orbitals. It is observed that the H contribution to the band structure (red in the pDOS) includes bands at ca. −2.5 and 4 eV. Sharing of electrons between the H(s) and Si(p) orbitals results in hybridization in the DOS, as indicated by the purple lines in the band structure. We find that H is bound to Si through the Si(p_z) orbitals.

We sought to determine the origin of the direct-like band gap behavior of silicane. Interestingly, the band structure does not agree with the results that are expected from the Brus equation,[89,90] which describes how the energies of bands with different effective masses change with confinement. Our results indicate that silicane's lighter, direct transition bands increase in energy more slowly than the heavier, indirect transition bands as confinement increases. We hypothesize that H

termination of Si-NSs causes the lighter bands to move down in energy relative to the CBM_M (Figure S34a,b). Interestingly, the frontier orbitals at the CMB_Γ exists around the H atoms (Figure 4d,e), but H contributions do not appear in the bands or DOS at either the CBM_Γ or CBM_M (Figure 4c). The electrons associated with the CBM_Γ that occupy the space around the H atoms likely result from the larger electronegativity of H relative to Si. We note that one aspect that is lacking in our computational model is the contributions of Si-NS edges, corners, and Cl termination to the optical properties; this should be a topic of future research.

■ CONCLUSION

In summary, we characterized the structural, compositional, and optical properties of Si-NSs obtained from deintercalating $CaSi_2$ using cold ($\sim$−30 °C) aqueous HCl. We determined that the Si-NSs consist of a buckled Si monolayer that is mostly monohydride terminated, resembling silicane, with a relatively small quantity of chloride and hydroxide termination. We also conclude that many features observed in Raman, solid-state NMR, EDS, and XRD arise from impurities that originate from the precursor. Thus, we advise that, when commercially sourced $CaSi_2$ is used, researchers should carefully and judiciously distinguish which properties arise from the impurities versus those of the Si-NSs. We determine that the relatively intense FTIR signals from oxygen-containing functional groups do not correlate to large amounts of oxidation, as the FTIR intensities cannot be quantitatively interpreted as concentration without knowing the absorption cross section or the Born effective charge tensors and atomic displacements associated with each vibrational mode. Our results from UV−visible absorbance measurements, steady-state PL, and time-resolved PL correlate well with DFT simulations and point toward direct-like band gap behavior. The Si-NSs have relatively short carrier lifetimes and blue-green PL with narrower line width in comparison to other forms of nano-Si such as Si nanocrystals or porous Si. This work elucidates the structure of deintercalated $CaSi_2$ by providing conclusive experimental data that is supported by DFT calculations. This new understanding may help guide the integration of Si-NSs into next-generation electronic, optoelectronic, and quantum devices.

■ EXPERIMENTAL METHODS

All data were collected under ambient conditions unless otherwise specified.

Chemicals. Calcium disilicide ($CaSi_2$, Sigma-Aldrich, technical grade), 36−38% hydrochloric acid (HCl(aq), Fisher, ACS plus grade), methanol (Sigma-Aldrich, ACS reagent grade), toluene (Sigma-Aldrich, anhydrous), acetone (Fisher, Certified ACS), isopropyl alcohol (Fisher, HPLC grade), detergent (Decon Contrex), and calcium chloride dihydrate ($CaCl_2$·$2H_2O$, Fisher, Certified ACS) were all used without any additional purification unless otherwise noted. Deionized water was obtained in house with a Milli-Q Advantage A10 Water Purification System with a resistivity of 18.2 MΩ●cm. Glass substrates were manufactured by Corning Eagle XG and purchased from Thin Film Devices. Carbon paint (DAG-T-502, Product No. 16056) was purchased from Ted Pella.

Synthesis of Si-NSs. In a glovebox filled with N_2, 1.707 g of $CaSi_2$ was placed in a round-bottom, three-necked flask that was attached to a Schlenk line using standard air-free techniques. In a separate flask, 142 mL of concentrated HCl(aq) was degassed via three freeze/pump/thaw cycles with liquid N_2. After the last thaw cycle, the HCl was chilled to −20 °C and injected into the flask containing the $CaSi_2$, after which the flask was immediately flushed with N_2. The reaction

mixture was initially chilled to −52 °C and held at $\sim$−30 °C. The contents of the flask were stirred for 5 days. Toward the end of the reaction, the temperature slowly increased to room temperature and the reaction mixture was exposed to air. The product was filtered in air via vacuum filtration through a fritted glass filter funnel (porosity of 10−15 μm) and washed with methanol to remove residual HCl, H_2O, and $CaCl_2$. After washing, the product was allowed to dry on the filter for $\sim$5 min, after which the product was dried under vacuum at room temperature for $\sim$20 min before moving to a glovebox filled with N_2 for characterization.

Solid-State Nuclear Magnetic Resonance. Solid-state NMR experiments were performed on a Bruker wide-bore 9.4 T ($\nu_0(^1H)$ = 400.5 MHz) NMR spectrometer equipped with a Bruker Avance III HD console, a Bruker 2.5 mm HXY MAS probe in the $^1H−^{13}C−^{29}Si$ configuration, and a Bruker 4 mm HX MAS probe in the $^1H−^{29}Si$ mode, and MAS rotors were spun with N_2 gas. The direct ^{29}Si excitation spectrum was performed on an Oxford wide-bore 9.4 T NMR spectrometer equipped with a Bruker Avance II console and a Bruker 4 mm HX probe in $^1H−^{29}Si$ double mode and spun with compressed air. All NMR experiments (except CP-INADEQUATE and direct ^{29}Si excitation) were acquired with a MAS frequency between 22 and 25 kHz, depending on the experiment; CP-INADEQUATE and direct ^{29}Si excitation experiments used a spinning frequency of 10 kHz on the 4 mm HX MAS probe. ^1H chemical shifts were referenced to neat tetramethylsilane, using the ^1H chemical shift of adamantane (^1H 1.82 ppm) as a secondary reference. ^{29}Si chemical shifts were indirectly referenced to established chemical shift standards using previously published relative NMR frequencies.[91] All NMR data except the ^{29}Si direct excitation were collected 1.5 months after the Si-NSs were isolated; the ^{29}Si direct excitation was collected 4.5 months after the Si-NSs were isolated. Additional details on solid-state NMR experiments are given in the Supporting Information.

Powder X-ray Diffraction. XRD patterns were collected with a Bruker DaVinci D8 Advance diffractometer with a Cu Kα radiation source. Powder was placed in an acrylic substrate in a glovebox filled with N_2 and subsequently sealed with a piece of Kapton tape to prevent oxidation during data acquisition, which occurred over the course of 24 h (range 3−80° 2θ, step size 0.0205° 2θ, at 22 s per step). Data were collected 3.8 months after the Si-NSs were isolated.

Transmission Electron Microscopy. TEM images were recorded using an FEI Tecnai G2-F20 instrument operated at 200 kV. TEM preparation was performed by sonicating the sample in degassed, anhydrous toluene before depositing on lacey carbon grids in a glovebox filled with N_2. Data were collected between 3.9 and 4.2 months after the Si-NSs were isolated.

Diffuse Reflectance. Diffuse reflectance data were collected with a PerkinElmer Lambda 750 spectrophotometer equipped with a Labsphere 100 mm integrating sphere; these data were transformed with the Kubelka−Munk equation. The sample was dispensed onto the adhesive side of clear packaging tape (3 M Scotch Packaging Tape), and the reflectance of the bare Si-NSs was taken. Data were collected 5.6 months after the Si-NSs were isolated.

Fourier Transform Infrared Spectroscopy. FTIR data were collected with a Nicolet iS5 FTIR spectrometer with an iD5 attenuated total reflectance (ATR) accessory. Data were collected 5.9 months after the Si-NSs were isolated.

Raman Spectroscopy. Raman spectra and bright-field optical microscopy images were collected using an XploRa Raman confocal upright microscope (HORIBA Scientific, Edison, NJ). Approximately 20 mg of the sample was placed onto lens paper positioned on top of a glass cover slide (to ensure the powder did not disperse across the bare glass). A 6.97 mW, 532 nm solid-state diode laser producing a 16.8 ± 0.3 μm laser spot size passing through a 300 μm confocal pinhole was focused on the sample surface by means of an Olympus 10× magnification objective (0.25 numerical aperture, Olympus, Melville, NY). The signal was collected by a Synapse EMCCD sensor operating at −70 °C with a grating of 1200 grooves/mm, allowing a spectral resolution of 5 cm^{-1}. The acquisition time was 60 s. Data were collected 3.7 months after the Si-NSs were isolated.

Thermogravimetric Analysis and Differential Scanning Calorimetry. TGA/DSC data were collected in an alumina (Al_2O_3) crucible, with a flow rate of 10 mL/min of either N_2 or synthetic air and a ramp rate of 10 °C/min. Synthetic air consisted of a blend of 20 mol % O_2 and 80 mol % N_2. The TGA/DSC instrument was a Netzsch Jupiter STA449 F1. The exhaust gases of the TGA/DSC were sent through FTIR and mass spectrometer (MS) instruments to analyze the gaseous decomposition byproducts. The FTIR was a Bruker Tensor 37 instrument, and the MS was an Aëolos QMS 403 D instrument. Data were collected 1.2 months after the Si-NSs were isolated.

Scanning Electron Microscopy. SEM images and energy dispersive X-ray spectroscopy (EDS) data were collected with an FEI Teneo instrument. Samples were prepared in a glovebox filled with N_2 by directly painting an aluminum SEM stub with carbon paint and immediately depositing the sample onto the wet carbon paint. The sample was kept under N_2 until immediately before loading into the SEM.

Photoluminescence. PL data were collected on a Horiba-Jobin Yvon Nanolog scanning spectrofluorometer using degassed, anhydrous methanol. The sample was prepared in a glovebox filled with N_2. Data were collected 5.2 months after the Si-NSs were isolated.

Time-Resolved Photoluminescence. TRPL lifetime measurements were performed using a custom-built confocal scanning microscope utilizing a time-correlated single photon counting method. Briefly, a 405 nm laser diode (QLD-405-100S, QPhotonics) with 4 ns pulse duration and a repetition rate of 1 MHz was used as the excitation source. TRPL was collected using a 50× long working distance objective in reflection geometry and filtered by a 500 nm long-pass filter and monochromator (NeoChromax 250, Dawool Attoics Co., Ltd.). Photons were counted with a Hamamatsu microchannel plate-photomultiplier tube (MCP-PMT). Samples were prepared in a glovebox filled with N_2 by drop-casting a suspension of the Si-NSs in anhydrous toluene onto a freshly cleaned glass substrate. Glass substrates were cleaned by ultrasonication in detergent water, followed by rinsing with deionized water and subsequent ultrasonication in acetone followed by isopropyl alcohol. Then, the substrates were blown dry with ultrahigh-purity N_2, followed by treatment with O_2 plasma. The substrates were then loaded into a glovebox. All three sonication steps were performed for 20 min each. Data were collected 5.0 months after the Si-NSs were isolated.

X-ray Photoelectron Spectroscopy. XPS measurements were performed using a Kratos Amicus/ESCA 3400 instrument. The sample was irradiated with 240 W unmonochromated Al Kα X-rays, and photoelectrons emitted at 0° from the surface normal were energy analyzed using a DuPont type analyzer. Data were collected 10.8 months after the Si-NSs were isolated.

COMPUTATIONAL METHODS

All calculations were performed via plane wave DFT in VASP,[43,44] and all structures were subject to the same computational treatment, unless otherwise specified, as described in the following. Exchange-correlation functionals were described by the PBE-GGA.[92] PAW[43,45,93] potentials approximated core electrons. Unit cell shape, volume, and atomic positions were relaxed (ISIF = 3) until all forces and the self-consistent field energies were less than 0.01 eV/Å and 1 × 10^{-5} eV, respectively. Brillouin zone k-point spacing was at most 0.13 Å^{-1} with an automatic Monkhorst–Pack grid.[94] Kinetic energy cutoffs were 550 eV. Raman, FTIR, extinction coefficients, band structures, and real-space orbitals were all calculated after geometric relaxation. Real-space orbitals and crystal structures were visualized with VESTA.[95] Band structures and projected densities of states (pDOS) were plotted in MATLAB using a custom-written code. Due to computational cost, calculations of FTIR, Raman, bands, pDOS, and orbitals were not performed on the finite NSs described in the Supporting Information (see **NMR 1**, **NMR 2**, and **NMR 3**).

Raman and FTIR. Raman spectra were simulated by calculating the off-resonance activity by calculating the phonons at the Γ point and subsequently calculating the macroscopic dielectric tensor with the vasp_raman.py script.[96] FTIR spectra were simulated with techniques described elsewhere.[72,97−101] FTIR and Raman peaks were fit to Lorentzian distributions with a fwhm of 30 cm^{-1}. To model the FTIR and Raman vibrational modes, calculations were performed on a total of five distinct models (Figure S24); four of the structures are infinite sheets, and one is semi-infinite. The semi-infinite sheet has at least 17 Å of vacuum between nearest-neighbor hydrogen atoms in the direction parallel to the sheet's surface; the z-direction was allowed to relax to an equilibrium nearest-neighbor distance. See the Supporting Information for additional details of these models. The amplitude of the vibrational modes in the GIFs are magnified by a factor of 10 to aid in visual clarity (see the Supporting Information).

Solid-State NMR. SSNMR calculations were performed using plane wave DFT with the gauge-including projector augmented wave (GIPAW)[102] approach using the commercially available software CASTEP version 2017 R2.[103] The geometry relaxation and NMR properties were calculated with the PBE-GGA[92] functional with On-the-Fly ultrasoft pseudopotential[104,105] and the ZORA[106] relativistic treatment. The kinetic energy cutoff was set to 630 eV with a Monkhorst−Pack grid with a k-point spacing of 0.03 Å^{-1}. Calculations were performed on a total of seven distinct structural models, three of the structures being finite silicane sheets with at least 14 Å of vacuum between nearest-neighbor hydrogen atoms in the directions parallel to the sheet (Figure S30) and four being infinite sheets (Figure S31). See the Supporting Information for additional details of these models.

■ ASSOCIATED CONTENT

ⓈSupporting Information

The Supporting Information is available free of charge at https://pubs.acs.org/doi/10.1021/acs.chemmater.9b04180.

> Solid-state NMR experimental details, TEM images, powder XRD patterns, SEM-EDS elemental mapping, Raman spectra, bright-field optical microscopy images, Raman and FTIR peak assignment tables, Born effective charge tensors, additional FTIR spectra, XPS spectra, TGA and DSC profiles coupled with FTIR and MS, associated XRD patterns after thermal decomposition, ball and stick models of DFT structures, DFT simulations of Raman and FTIR, additional NMR spectra, NMR calibration curve, Tauc plots of KM data, band structures with pDOS of silicon, silicane, and *cis*-hydroxysilicane, and energies of the relaxed structures (PDF)

> VASP output files of Raman/FTIR calculations (ZIP)

> CASTEP output files of NMR calculations (ZIP)

> GIF files which illustrate the vibrational modes (ZIP)

■ AUTHOR INFORMATION

Corresponding Author

E-mail for M.G.P.: panthani@iastate.edu.

ORCID Ⓘ

Bradley J. Ryan: 0000-0002-7719-5593

Rainie D. Nelson: 0000-0003-1335-0002

Luke T. Roling: 0000-0001-9742-2573

Emily A. Smith: 0000-0001-7438-7808

Aaron J. Rossini: 0000-0002-1679-9203

Matthew G. Panthani: 0000-0002-3795-2051

Author Contributions

⊥Y.W. and U.R. contributed equally to this work.

Notes

The authors declare no competing financial interest.

REFERENCES

(1) Novoselov, K. S.; Geim, A. K.; Morozov, S. V.; Jiang, D.; Zhang, Y.; Dubonos, S. V.; Grigorieva, I. V.; Firsov, A. A. Electric Field Effect in Atomically Thin Carbon Films. *Science* **2004**, *306* (5696), 666–669.

(2) Li, X.; Zhu, H. Two-Dimensional MoS_2: Properties, Preparation, and Applications. *J. of Materiomics* **2015**, *1* (1), 33–44.

(3) Nakano, H.; Nakano, M.; Nakanishi, K.; Tanaka, D.; Sugiyama, Y.; Ikuno, T.; Okamoto, H.; Ohta, T. Preparation of Alkyl-Modified Silicon Nanosheets by Hydrosilylation of Layered Polysilane (Si_6H_6). *J. Am. Chem. Soc.* **2012**, *134* (12), 5452–5455.

(4) Splendiani, A.; Sun, L.; Zhang, Y.; Li, T.; Kim, J.; Chim, C.-Y.; Galli, G.; Wang, F. Emerging Photoluminescence in Monolayer MoS_2. *Nano Lett.* **2010**, *10* (4), 1271–1275.

(5) Mina, A. N.; Awadallah, A. A.; Phillips, A. H.; Ahmed, R. R. Simulation of the Band Structure of Graphene and Carbon Nanotube. *J. Phys.: Conf. Ser.* **2012**, *343* (1), No. 012076.

(6) Robert, C.; Lagarde, D.; Cadiz, F.; Wang, G.; Lassagne, B.; Amand, T.; Balocchi, A.; Renucci, P.; Tongay, S.; Urbaszek, B.; et al. Exciton Radiative Lifetime in Transition Metal Dichalcogenide Monolayers. *Phys. Rev. B: Condens. Matter Mater. Phys.* **2016**, *93* (20), 205423.

(7) Gan, L.; Li, J.; Fang, Z.; He, H.; Ye, Z. Effects of Organic Cation Length on Exciton Recombination in Two-Dimensional Layered Lead Iodide Hybrid Perovskite Crystals. *J. Phys. Chem. Lett.* **2017**, *8* (20), 5177–5183.

(8) Butler, S. Z.; Hollen, S. M.; Cao, L.; Cui, Y.; Gupta, J. A.; Gutiérrez, H. R.; Heinz, T. F.; Hong, S. S.; Huang, J.; Ismach, A. F.; et al. Progress, Challenges, and Opportunities in Two-Dimensional Materials Beyond Graphene. *ACS Nano* **2013**, *7* (4), 2898–2926.

(9) Pulci, O.; Gori, P.; Marsili, M.; Garbuio, V.; Sole, R. D.; Bechstedt, F. Strong Excitons in Novel Two-Dimensional Crystals: Silicane and Germanane. *EPL* **2012**, *98* (3), 37004.

(10) Brandt, M. S.; Breitschwerdt, A.; Fuchs, H. D.; Höpner, A.; Rosenbauer, M.; Stutzmann, M.; Weber, J. New Growth Technique for Luminescent Layers on Silicon. *Appl. Phys. A: Solids Surf.* **1992**, *54* (6), 567–569.

(11) Nakano, H.; Ishii, M.; Nakamura, H. Preparation and Structure of Novel Siloxene Nanosheets. *Chem. Commun.* **2005**, *0* (23), 2945–2947.

(12) Weiss, A.; Beil, G.; Meyer, H. The Topochemical Reaction of $CaSi_2$ to a Two-Dimensional Subsiliceous Acid $Si_6H_3(OH)_3$ (= Kautskys' Siloxene). *Z. Naturforsch., B: J. Chem. Sci.* **1980**, *35* (1), 25–30.

(13) Deák, P.; Rosenbauer, M.; Stutzmann, M.; Weber, J.; Brandt, M. S. Siloxene: Chemical Quantum Confinement Due to Oxygen in a Silicon Matrix. *Phys. Rev. Lett.* **1992**, *69* (17), 2531–2534.

(14) Wöhler, F. Ueber Verbindungen Des Siliciums Mit Sauerstoff Und Wasserstoff. *Justus Liebigs Annalen der Chemie* **1863**, *127* (3), 257–274.

(15) Kautsky, H. Über Einige Ungesättigte Siliciumverbindungen. *Zeitschrift für anorganische und allgemeine Chemie* **1921**, *117* (1), 209–242.

(16) Kautsky, H.; Vogell, W.; Oeters, F. Notizen: Die Bedeutung Elektronenmikroskopischer Untersuchungen Für Die Konstitutions- Und Strukturaufklärung Des Siloxens. *Z. Naturforsch., B: J. Chem. Sci.* **1955**, *10* (10), 597–598.

(17) Karar, D.; Bandyopadhyay, N. R.; Pramanick, A. K.; Acharyya, D.; Conibeer, G.; Banerjee, N.; Kusmartseva, O. E.; Ray, M. Quasi-Two-Dimensional Luminescent Silicon Nanosheets. *J. Phys. Chem. C* **2018**, *122* (33), 18912–18921.

(18) Krishnamoorthy, K.; Pazhamalai, P.; Kim, S.-J. Two-Dimensional Siloxene Nanosheets: Novel High-Performance Supercapacitor Electrode Materials. *Energy Environ. Sci.* **2018**, *11* (6), 1595–1602.

(19) Li, S.; Wang, H.; Li, D.; Zhang, X.; Wang, Y.; Xie, J.; Wang, J.; Tian, Y.; Ni, W.; Xie, Y. Siloxene Nanosheets: A Metal-Free Semiconductor for Water Splitting. *J. Mater. Chem. A* **2016**, *4* (41), 15841–15844.

(20) Helbich, T.; Lyuleeva, A.; Ludwig, T.; Scherf, L. M.; Fässler, T. F.; Lugli, P.; Rieger, B. One-Step Synthesis of Photoluminescent Covalent Polymeric Nanocomposites from 2D Silicon Nanosheets. *Adv. Funct. Mater.* **2016**, *26* (37), 6711–6718.

(21) Lyuleeva, A.; Helbich, T.; Rieger, B.; Lugli, P. Polymer-Silicon Nanosheet Composites: Bridging the Way to Optoelectronic Applications. *J. Phys. D: Appl. Phys.* **2017**, *50* (13), 135106.

(22) Ohshita, J.; Yamamoto, K.; Tanaka, D.; Nakashima, M.; Kunugi, Y.; Ohashi, M.; Nakano, H. Preparation and Photocurrent Generation of Silicon Nanosheets with Aromatic Substituents on the Surface. *J. Phys. Chem. C* **2016**, *120* (20), 10991–10996.

(23) Helbich, T.; Lyuleeva, A.; Höhlein, I. M. D.; Marx, P.; Scherf, L. M.; Kehrle, J.; Fässler, T. F.; Lugli, P.; Rieger, B. Radical-Induced Hydrosilylation Reactions for the Functionalization of Two-Dimensional Hydride Terminated Silicon Nanosheets. *Chem. - Eur. J.* **2016**, *22* (18), 6194–6198.

(24) Okamoto, H.; Kumai, Y.; Sugiyama, Y.; Mitsuoka, T.; Nakanishi, K.; Ohta, T.; Nozaki, H.; Yamaguchi, S.; Shirai, S.; Nakano, H. Silicon Nanosheets and Their Self-Assembled Regular Stacking Structure. *J. Am. Chem. Soc.* **2010**, *132* (8), 2710–2718.

(25) Pazhamalai, P.; Krishnamoorthy, K.; Sahoo, S.; Mariappan, V. K.; Kim, S.-J. Understanding the Thermal Treatment Effect of Two-Dimensional Siloxene Sheets and the Origin of Superior Electrochemical Energy Storage Performances. *ACS Appl. Mater. Interfaces* **2019**, *11* (1), 624–633.

(26) Zhang, F.-B.; Lv, S.-F.; Jiang, J.-X.; Ni, Y. Preparation of Siloxene Nanosheet-Supported Palladium as Sustainable Catalyst for Mizoroki−Heck Reaction. *Appl. Organomet. Chem.* **2014**, *28* (11), 826−830.

(27) Todori, K.; Hayase, S. Similarities and Differences of Phonon Modes in Silicon Materials Depending on Dimension: Raman Spectroscopy of Polysilanes and Siloxene. *Phys. B* **1996**, *219−220*, 514−516.

(28) Molassioti-dohms, A.; Dettlaff-weglikowska, U.; Finkbeiner, S.; Hönle, W.; Weber, J. Photo- and Chemiluminescence from Wöhler Siloxenes. *J. Electrochem. Soc.* **1996**, *143* (8), 2674−2677.

(29) Brandt, M. S.; Stutzmann, M. Triplet Excitons in Porous Silicon and Siloxene. *Solid State Commun.* **1995**, *93* (6), 473−477.

(30) Dahn, J. R.; Way, B. M.; Fuller, E. W.; Weydanz, W. J.; Tse, J. S.; Klug, D. D.; Van Buuren, T.; Tiedje, T. X-ray Diffraction and X-ray Absorption Studies of Porous Silicon, Siloxene, Heat-treated Siloxene, and Layered Polysilane. *J. Appl. Phys.* **1994**, *75* (4), 1946−1951.

(31) Stutzmann, M.; Brandt, M. S.; Rosenbauer, M.; Weber, J.; Fuchs, H. D. Photoluminescence Excitation Spectroscopy of Porous Silicon and Siloxene. *Phys. Rev. B: Condens. Matter Mater. Phys.* **1993**, *47* (8), 4806−4809.

(32) Stutzmann, M.; Brandt, M. S.; Rosenbauer, M.; Fuchs, H. D.; Finkbeiner, S.; Weber, J.; Deak, P. Luminescence and Optical Properties of Siloxene. *J. Lumin.* **1993**, *57* (1), 321−330.

(33) Friedman, S. L.; Marcus, M. A.; Adler, D. L.; Xie, Y.-H.; Harris, T. D.; Citrin, P. H. Unimportance of Siloxene in the Luminescence of Porous Silicon. *Appl. Phys. Lett.* **1993**, *62* (16), 1934−1936.

(34) Dahn, J. R.; Way, B. M.; Fuller, E.; Tse, J. S. Structure of Siloxene and Layered Polysilane (Si$_6$H$_6$). *Phys. Rev. B: Condens. Matter Mater. Phys.* **1993**, *48* (24), 17872−17877.

(35) Fuchs, H. D.; Stutzmann, M.; Brandt, M. S.; Rosenbauer, M.; Weber, J.; Cardona, M. Visible Luminescence from Porous Silicon and Siloxene. *Phys. Scr.* **1992**, *T45*, 309.

(36) Okamoto, H.; Sugiyama, Y.; Nakanishi, K.; Ohta, T.; Mitsuoka, T.; Nakano, H. Surface Modification of Layered Polysilane with N-Alkylamines, α,ω-Diaminoalkanes, and ω-Aminocarboxylic Acids. *Chem. Mater.* **2015**, *27* (4), 1292−1298.

(37) Kumai, Y.; Nakano, H. Characteristics of Layered Polysilane and Its Application to Lithium Ion Battery Anodes. *Jpn. J. Appl. Phys.* **2015**, *54* (3), No. 035201.

(38) Kumai, Y.; Shirai, S.; Sudo, E.; Seki, J.; Okamoto, H.; Sugiyama, Y.; Nakano, H. Characteristics and Structural Change of Layered Polysilane (Si$_6$H$_6$) Anode for Lithium Ion Batteries. *J. Power Sources* **2011**, *196* (3), 1503−1507.

(39) Kumai, Y.; Shirai, S.; Okamoto, H.; Sugiyama, Y.; Nakano, H. Properties and Mechanism of Layered Polysilane (Si$_6$H$_6$) Anode. *IOP Conf. Ser.: Mater. Sci. Eng.* **2011**, *18* (12), 122005.

(40) Yamanaka, S.; Matsu-ura, H.; Ishikawa, M. New Deintercalation Reaction of Calcium from Calcium Disilicide. Synthesis of Layered Polysilane. *Mater. Res. Bull.* **1996**, *31* (3), 307−316.

(41) Nishimura, K.; Nagao, Y.; Yamanaka, S.; Matsu-ura, H. Characterization of Layered Polysilane. *Jpn. J. Appl. Phys.* **1996**, *35* (3A), L293.

(42) Kohn, W.; Sham, L. J. Self-Consistent Equations Including Exchange and Correlation Effects. *Phys. Rev.* **1965**, *140* (4A), A1133−A1138.

(43) Kresse, G.; Furthmüller, J. Efficient Iterative Schemes for Ab Initio Total-Energy Calculations Using a Plane-Wave Basis Set. *Phys. Rev. B: Condens. Matter Mater. Phys.* **1996**, *54* (16), 11169−11186.

(44) Kresse, G.; Furthmüller, J. Efficiency of Ab-Initio Total Energy Calculations for Metals and Semiconductors Using a Plane-Wave Basis Set. *Comput. Mater. Sci.* **1996**, *6* (1), 15−50.

(45) Kresse, G.; Joubert, D. From Ultrasoft Pseudopotentials to the Projector Augmented-Wave Method. *Phys. Rev. B: Condens. Matter Mater. Phys.* **1999**, *59* (3), 1758−1775.

(46) Bianco, E.; Butler, S.; Jiang, S.; Restrepo, O. D.; Windl, W.; Goldberger, J. E. Stability and Exfoliation of Germanane: A Germanium Graphane Analogue. *ACS Nano* **2013**, *7* (5), 4414−4421.

(47) Fuchs, H. D.; Stutzmann, M.; Brandt, M. S.; Rosenbauer, M.; Weber, J.; Breitschwerdt, A.; Deák, P.; Cardona, M. Porous Silicon and Siloxene: Vibrational and Structural Properties. *Phys. Rev. B: Condens. Matter Mater. Phys.* **1993**, *48* (11), 8172−8189.

(48) Meng, X.; Sasaki, K.; Sano, K.; Yuan, P.; Tatsuoka, H. Synthesis of Crystalline Si-Based Nanosheets by Extraction of Ca from CaSi2 in Inositol Hexakisphosphate Solution. *Jpn. J. Appl. Phys.* **2017**, *56* (5S1), No. 05DE02.

(49) Brodsky, M. H.; Cardona, M.; Cuomo, J. J. Infrared and Raman Spectra of the Silicon-Hydrogen Bonds in Amorphous Silicon Prepared by Glow Discharge and Sputtering. *Phys. Rev. B* **1977**, *16* (8), 3556−3571.

(50) Durig, J. R.; Sullivan, J. F.; Qtaitat, M. A. Infrared and Raman Spectra, Conformational Stability, Barriers to Internal Rotation, Ab Initio Calculations, Ro Structure, and Vibrational Assignment for Methyl Vinyl Silane. *J. Mol. Struct.* **1991**, *243* (3), 239−273.

(51) Cardona, M. Vibrations in Amorphous Silicon and Its Alloys. *J. Mol. Struct.* **1986**, *141*, 93−107.

(52) Johnson, E. V.; Kroely, L.; Roca i Cabarrocas, P. Raman Scattering Analysis of SiH Bond Stretching Modes in Hydrogenated Microcrystalline Silicon for Use in Thin-Film Photovoltaics. *Sol. Energy Mater. Sol. Cells* **2009**, *93* (10), 1904−1906.

(53) Kanellis, G.; Morhange, J. F.; Balkanski, M. Effect of Dimensions on the Vibrational Frequencies of Thin Slabs of Silicon. *Phys. Rev. B: Condens. Matter Mater. Phys.* **1980**, *21* (4), 1543−1548.

(54) Uchinokura, K.; Sekine, T.; Matsuura, E. Raman Scattering by Silicon. *Solid State Commun.* **1972**, *11* (1), 47−49.

(55) Parker, J. H.; Feldman, D. W.; Ashkin, M. Raman Scattering by Silicon and Germanium. *Phys. Rev.* **1967**, *155* (3), 712−714.

(56) Quiroga-González, E.; Carstensen, J.; Glynn, C.; O'Dwyer, C.; Föll, H. Pore Size Modulation in Electrochemically Etched Macroporous P-Type Silicon Monitored by FFT Impedance Spectroscopy and Raman Scattering. *Phys. Chem. Chem. Phys.* **2014**, *16* (1), 255−263.

(57) Hessel, C. M.; Wei, J.; Reid, D.; Fujii, H.; Downer, M. C.; Korgel, B. A. Raman Spectroscopy of Oxide-Embedded and Ligand-Stabilized Silicon Nanocrystals. *J. Phys. Chem. Lett.* **2012**, *3* (9), 1089−1093.

(58) Galeener, F. L.; Mikkelsen, J. C. Raman Studies of the Thermal Oxide of Silicon. *Solid State Commun.* **1981**, *37* (9), 719−723.

(59) Walrafen, G. E. Raman Spectra from Si−OH Groups in Solid Optical Fibers. *J. Chem. Phys.* **1975**, *62* (1), 297−298.

(60) Kalem, S.; Chevallier, J.; Al Dallal, S.; Bourneix, J. Infrared Vibrational Spectra of Chlorinated and Hydrogenated Amorphous Silicon. *J. de Physique Colloques* **1981**, *42* (C4), C4-361−C4-363.

(61) Brandt, M. S.; Fuchs, H. D.; Stutzmann, M.; Weber, J.; Cardona, M. The Origin of Visible Luminescence from "Porous Silicon": A New Interpretation. *Solid State Commun.* **1992**, *81* (4), 307−312.

(62) Zamanzadeh-Hanebuth, N.; Brandt, M. S.; Stutzmann, M. Vibrational Properties of Siloxene: Isotope Substitution Studies. *J. Non-Cryst. Solids* **1998**, *227−230*, 503−506.

(63) Dasog, M.; Yang, Z.; Veinot, J. G. C. Size-Controlled Solid State Synthesis of Luminescent Silicon Nanocrystals Using Stöber Silica Particles. *CrystEngComm* **2012**, *14* (22), 7576−7578.

(64) Infrared Spectroscopy of Thin Layers in Silicon Microelectronics. In *Handbook of Infrared Spectroscopy of Ultrathin Films*; Wiley: 2003; pp 416−475.

(65) Thissen, P.; Peixoto, T.; Longo, R. C.; Peng, W.; Schmidt, W. G.; Cho, K.; Chabal, Y. J. Activation of Surface Hydroxyl Groups by Modification of H-Terminated Si(111) Surfaces. *J. Am. Chem. Soc.* **2012**, *134* (21), 8869−8874.

(66) Torun, B.; Kunze, C.; Zhang, C.; Kühne, T. D.; Grundmeier, G. Study of Water Adsorption and Capillary Bridge Formation for SiO$_2$ Nanoparticle Layers by Means of a Combined in Situ FT-IR Reflection Spectroscopy and QCM-D Set-Up. *Phys. Chem. Chem. Phys.* **2014**, *16* (16), 7377−7384.

(67) Walrafen, G. E.; Blatz, L. A. Weak Raman Bands from Water. *J. Chem. Phys.* **1973**, *59* (5), 2646−2650.

(68) Mawhinney, D. B.; Glass, J. A.; Yates, J. T. FTIR Study of the Oxidation of Porous Silicon. *J. Phys. Chem. B* **1997**, *101* (7), 1202–1206.

(69) Michalak, D. J.; Rivillon, S.; Chabal, Y. J.; Estève, A.; Lewis, N. S. Infrared Spectroscopic Investigation of the Reaction of Hydrogen-Terminated, (111)-Oriented, Silicon Surfaces with Liquid Methanol. *J. Phys. Chem. B* **2006**, *110* (41), 20426–20434.

(70) Islam, M. A.; Purkait, T. K.; Veinot, J. G. C. Chloride Surface Terminated Silicon Nanocrystal Mediated Synthesis of Poly(3-Hexylthiophene). *J. Am. Chem. Soc.* **2014**, *136* (43), 15130–15133.

(71) Uriarte, L. M.; Dubessy, J.; Boulet, P.; Baonza, V. G.; Bihannic, I.; Robert, P. Reference Raman spectra of synthesized $CaCl_2 \cdot nH_2O$ solids (n = 0, 2, 4, 6). *J. Raman Spectrosc.* **2015**, *46*, 822–828.

(72) Esfarjani, K.; Hashi, Y.; Onoe, J.; Takeuchi, K.; Kawazoe, Y. Vibrational Modes and IR Analysis of Neutral Photopolymerized C_{60} Dimers. *Phys. Rev. B: Condens. Matter Mater. Phys.* **1998**, *57* (1), 223–229.

(73) Born, M.; Huang, K. *Dynamical Theory of Crystal Lattices*; Oxford University Press: Oxford, U.K., 1954.

(74) Hanrahan, M. P.; Fought, E. L.; Windus, T. L.; Wheeler, L. M.; Anderson, N. C.; Neale, N. R.; Rossini, A. J. Characterization of Silicon Nanocrystal Surfaces by Multidimensional Solid-State NMR Spectroscopy. *Chem. Mater.* **2017**, *29* (24), 10339–10351.

(75) Neiner, D.; Kauzlarich, S. M. Hydrogen-Capped Silicon Nanoparticles as a Potential Hydrogen Storage Material: Synthesis, Characterization, and Hydrogen Release. *Chem. Mater.* **2010**, *22* (2), 487–493.

(76) Lee, D.; Kaushik, M.; Coustel, R.; Chenavier, Y.; Chanal, M.; Bardet, M.; Dubois, L.; Okuno, H.; Rochat, N.; Duclairoir, F.; et al. Solid-State NMR and DFT Combined for the Surface Study of Functionalized Silicon Nanoparticles. *Chem. - Eur. J.* **2015**, *21* (45), 16047–16058.

(77) Schnell, I.; Spiess, H. W. High-Resolution ¹H NMR Spectroscopy in the Solid State: Very Fast Sample Rotation and Multiple-Quantum Coherences. *J. Magn. Reson.* **2001**, *151* (2), 153–227.

(78) Elena, B.; Lesage, A.; Steuernagel, S.; Böckmann, A.; Emsley, L. Proton to Carbon-13 INEPT in Solid-State NMR Spectroscopy. *J. Am. Chem. Soc.* **2005**, *127* (49), 17296–17302.

(79) Hahn, J. Beiträge Zur Chemie Des Silieiums Und Germaniums, XXIX [1] ²⁹Si-NMR-Spektroskopische Untersuchungen von Geradkettigen Und Verzweigten Silanen/Contributions to the Chemistry of Silicon and Germanium, XXIX [1] ²⁹Si NMR Spectroscopic Investigations on Straight and Branched Silanes. *Z. Naturforsch., B: J. Chem. Sci.* **1980**, *35* (3), 282–296.

(80) Tsuboi, T.; Sakka, T.; Ogata, Y. H. Structural Study of Porous Silicon and Its Oxidized States by Solid-State High-Resolution ²⁹Si NMR Spectroscopy. *Phys. Rev. B: Condens. Matter Mater. Phys.* **1998**, *58* (20), 13863–13869.

(81) Lesage, A.; Auger, C.; Caldarelli, S.; Emsley, L. Determination of Through-Bond Carbon–Carbon Connectivities in Solid-State NMR Using the INADEQUATE Experiment. *J. Am. Chem. Soc.* **1997**, *119* (33), 7867–7868.

(82) Ohashi, M.; Yaokawa, R.; Takatani, Y.; Nakano, H. Versatile Reducing Reaction Field within Layered Polysilane for Efficient One-Pot Synthesis of Metal Nanoparticles. *ChemNanoMat* **2017**, *3* (8), 534–537.

(83) Atsalakis, A.; Tsetseris, L. First-Principles Study of Siloxene and Germoxene: Stable Conformations, Electronic Properties, and Defects. *J. Phys.: Condens. Matter* **2014**, *26* (28), 285301.

(84) Van de Walle, C. G.; Northrup, J. E. First-Principles Investigation of Visible Light Emission from Silicon-Based Materials. *Phys. Rev. Lett.* **1993**, *70* (8), 1116–1119.

(85) Takeda, K.; Shiraishi, K. Electronic Structure of Silicon-Oxygen High Polymers. *Solid State Commun.* **1993**, *85* (4), 301–305.

(86) Gao, N.; Tao Zheng, W.; Jiang, Q. Density Functional Theory Calculations for Two-Dimensional Silicene with Halogen Functionalization. *Phys. Chem. Chem. Phys.* **2012**, *14* (1), 257–261.

(87) Zhang, W.-B.; Song, Z.-B.; Dou, L.-M. The Tunable Electronic Structure and Mechanical Properties of Halogenated Silicene: A First-Principles Study. *J. Mater. Chem. C* **2015**, *3* (13), 3087–3094.

(88) Liu, Z.; Bhamu, K. C.; Luo, L.; Shah, S.; Park, J.-M.; Cheng, D.; Long, M.; Biswas, R.; Fungara, F.; Shinar, R.; et al. Spatial–Temporal Spectroscopy Characterizations and Electronic Structure of Methyl-ammonium Perovskites. *MRS Commun.* **2018**, *8* (3), 961–969.

(89) Brus, L. Electronic Wave Functions in Semiconductor Clusters: Experiment and Theory. *J. Phys. Chem.* **1986**, *90* (12), 2555–2560.

(90) Williamson, A. J.; Franceschetti, A.; Fu, H.; Wang, L. W.; Zunger, A. Indirect Band Gaps in Quantum Dots Made from Direct-Gap Bulk Materials. *J. Electron. Mater.* **1999**, *28* (5), 414–425.

(91) Harris, R. K.; Becker, E. D.; De Menezes, S. M. C.; Goodfellow, R.; Granger, P. NMR Nomenclature. Nuclear Spin Properties and Conventions for Chemical Shifts - (IUPAC Recommendations 2001). *Pure Appl. Chem.* **2001**, *73*, 1795–1818.

(92) Perdew, J. P.; Burke, K.; Ernzerhof, M. Generalized Gradient Approximation Made Simple. *Phys. Rev. Lett.* **1996**, *77* (18), 3865–3868.

(93) Blöchl, P. E. Projector Augmented-Wave Method. *Phys. Rev. B: Condens. Matter Mater. Phys.* **1994**, *50* (24), 17953–17979.

(94) Monkhorst, H. J.; Pack, J. D. Special Points for Brillouin-Zone Integrations. *Phys. Rev. B* **1976**, *13* (12), 5188–5192.

(95) Momma, K.; Izumi, F. VESTA: A Three-Dimensional Visualization System for Electronic and Structural Analysis. *J. Appl. Crystallogr.* **2008**, *41* (3), 653–658.

(96) Fonari, A.; Stauffer, S. *Vasp_raman.Py*; https://github.com/raman-sc/VASP/, 2013.

(97) Karhánek, D.; Bučko, T.; Hafner, J. A Density-Functional Study of the Adsorption of Methane-Thiol on the (111) Surfaces of the Ni-Group Metals: II. Vibrational Spectroscopy. *J. Phys.: Condens. Matter* **2010**, *22* (26), 265006.

(98) Karhánek, D. Self-Assembled Monolayers Studied by Density-Functional Theory. Ph.D. Dissertation, Universität Wien, Vienna, Austria, 2010.

(99) Baroni, S.; de Gironcoli, S.; Dal Corso, A.; Giannozzi, P. Phonons and Related Crystal Properties from Density-Functional Perturbation Theory. *Rev. Mod. Phys.* **2001**, *73* (2), 515–562.

(100) Giannozzi, P.; Baroni, S. Vibrational and Dielectric Properties of C60 from Density-functional Perturbation Theory. *J. Chem. Phys.* **1994**, *100* (11), 8537–8539.

(101) Karhánek, D. Calculation of vibrational (IR) intensities, https://homepage.univie.ac.at/david.karhanek/downloads.html (accessed Sep 18, 2017).

(102) Pickard, C. J.; Mauri, F. All-Electron Magnetic Response with Pseudopotentials: NMR Chemical Shifts. *Phys. Rev. B: Condens. Matter Mater. Phys.* **2001**, *63* (24), 245101.

(103) Clark, S. J.; Segall, M. D.; Pickard, C. J.; Hasnip, P. J.; Probert, M. I. J.; Refson, K.; Payne, M. C. First Principles Methods Using CASTEP. *Z. Kristallogr. - Cryst. Mater.* **2005**, *220* (5/6), 1.

(104) Vanderbilt, D. Soft Self-Consistent Pseudopotentials in a Generalized Eigenvalue Formalism. *Phys. Rev. B: Condens. Matter Mater. Phys.* **1990**, *41* (11), 7892–7895.

(105) Yates, J. R.; Pickard, C. J.; Mauri, F. Calculation of NMR Chemical Shifts for Extended Systems Using Ultrasoft Pseudopotentials. *Phys. Rev. B: Condens. Matter Mater. Phys.* **2007**, *76* (2), 024401.

(106) Green, T. F. G.; Yates, J. R. Relativistic Nuclear Magnetic Resonance J-Coupling with Ultrasoft Pseudopotentials and the Zeroth-Order Regular Approximation. *J. Chem. Phys.* **2014**, *140* (23), 234106.